Magnetic 3d–4f Chiral Clusters Showing Multimetal Site Magneto-Chiral Dichroism

Xing Wang, Shi-Qiang Wang, Jia-Nan Chen, Jian-Hua Jia, Cheng Wang, Kevin Paillot, Ivan Breslavetz, La-Sheng Long, Lansun Zheng, Geert Rikken, et al.

Magnetic 3d-4f Chiral Clusters Showing Multi-Metal Site Magneto-Chiral Dichroism

Xing Wang,[1,†] Shi-Qiang Wang,[1,†] Jia-Nan Chen,[1] Jian-Hua Jia,[2] Cheng Wang,[1] Kevin Paillot,[3] Ivan Breslavetz,[3] La-Sheng Long,[1] Lansun Zheng,[1] Geert L. J. A. Rikken,[3] Cyrille Train,[3] Xiang-Jian Kong[1,*] and Matteo Atzori[3,*]

[1] Collaborative Innovation Center of Chemistry for Energy Materials State Key Laboratory of Physical Chemistry of Solid Surfaces and Department of Chemistry, College of Chemistry and Chemical Engineering, Xiamen University, Xiamen (361005), China.

[2] Key Laboratory of Bioinorganic and Synthetic Chemistry of Ministry of Education, School of Chemistry, Sun Yat-Sen University, Guangzhou (510275), China.

[3] Laboratoire National des Champs Magnétiques Intenses (LNCMI), Univ. Grenoble Alpes, INSA Toulouse, Univ. Toulouse Paul Sabatier, EMFL, CNRS, (F-38042) Grenoble, France.

ABSTRACT: Here we report the molecular self-assembly of hydroxido-bridged $\{Ln_5Ni_6\}$ ($(Ln^{3+} = Dy^{3+}, Y^{3+})$ metal clusters by reaction of enantiopure chiral ligands, namely (*R*/*S*)-(2-hydroxy-3-methoxybenzyl)-serine) with Ni^{II} and Ln^{III} precursors. Single-crystal diffraction analysis reveals that these compounds are isostructural sandwich-like *3d-4f* heterometallic clusters showing helical chirality. Direct current magnetic measurements on $\{Dy_5Ni_6\}$ indicates ferromagnetic coupling between Dy^{III} and Ni^{II} centers, whereas those on $\{Y_5Ni_6\}$ denote that the Ni^{II} centers are antiferromagnetically coupled and/or magnetically anisotropic. Magneto-Chiral Dichroism (MChD) measurements on $\{Dy_5Ni_6\}$ and its comparison to that of $\{Y_5Ni_6\}$ provide the first experimental observation of intense multi-metal site MChD signals in the Visible-Near Infrared region. Moreover, the comparison of MChD with Natural and Magnetic Circular Dichroism spectra unambiguously demonstrate for the first time that the MChD signals associated with the Ni^{II} *d-d* transitions are mostly driven by natural optical activity and those associated with the Dy^{III} *f-f* transitions are driven by magnetic optical activity.

INTRODUCTION

Molecular materials showing synergy between chirality and magnetism offer a playground for the conception and the realization of functional materials for magneto-optical applications.[1–10] For two decades, acentric molecular magnetic systems raise a constant interest in molecular magnetism for two main reasons.[11] First, obtaining such materials, in particular in their two enantiomeric forms, represents a synthetic challenge. Second, these materials are at the origin of three physical properties, Magnetization-Induced Second Harmonic Generation (MSHG),[2,12] Multiferroicity,[9,13] and Magneto-Chiral Dichroism (MChD),[7] that are unique examples of a real synergy between low-symmetry related properties and magnetism. This opens new avenues for magneto-optical memories, optoelectronic and spintronic devices. To reach these objectives, it is fundamental to have a comprehension of these phenomena at the microscopic level.

MChD has been at first theoretically predicted[14–18] and then experimentally observed [14,19–23] as a bilinear effect that depends on the relative orientation (parallel or antiparallel) of the light wavevector ***k*** and the magnetic field pseudovector ***B***, and the intrinsic chirality of the material. It results in an enantioselective differential absorption or emission of light whose intensity is magnetization-dependent. Therefore, it can be potentially used for the optical readout of magnetic information stored in magnetic materials.[6,22] Indeed, it has been proposed, but not yet demonstrated, that an intense enough, close to 10%, MChD response might be used for the optical readout of magnetic data.[6] A principle similar to what is currently done with circularly polarized light in magnetooptical disk based on conventional inorganic materials can be envisioned with MChD using molecular systems able to retain the magnetization and a simpler and easily accessible unpolarized light source. For this reason, this effect has been searched in molecule-based magnets below their ordering temperatures,[3,24–26] and should further be investigated in lanthanide-based clusters exhibiting opened hysteresis cycles.

From the 1990s, discrete molecular systems, called single-molecule magnets (SMMs) have been proposed as potential materials from ultimate data storage and processing.[27] Owing to the central role of magnetic anisotropy on SMMs properties, the research in this domain is currently dominated by lanthanide-based systems with a definitive emphasis on Dy^{III} and Tb^{III} containing systems.[28,29] Chirality has been introduced in such systems in order to modulate their anisotropy[30–34] whereas complementary spin-carriers,[35–37] transition metal ions and/or radicals, were combined with lanthanide ions for a still elusive improvements of their magnetic properties.

Although Eu^{III} complexes were at the origin of the first experimental demonstration of MChD,[19] to date, this light-matter interaction has been studied in a limited number of lanthanide-based systems.[19,21,38,39] The association of *3d* and *4f* metal ions to study MChD appears particularly appealing since strong MChD signals were observed for both octahedrally coordinated Ni^{II} and for Ln^{III} complexes.[19–21,38,39] Nonetheless, a single heterometallic *3d-4f* chiral cluster containing Ni^{II} and Tb^{III} was investigated so far in the hard X-rays range of the electromagnetic spectrum revealing a low resolution MChD signal associated to the Tb^{III} X-ray absorption.[22] The absence of MChD signals at the Ni^{II} edge and temperature and magnetic field dependent studies strongly limits our understanding of such physico-chemical phenomenon.

To identify and understand the chemical and physico-chemical ingredients that drive strong MChD signals in complex chiral molecular systems, here we present a complete study of new chiral heterometallic clusters featuring enantiopure ligands and Ni^{II} and Dy^{III} ions, formulated as $[Ln_5Ni_6(R/S\text{-}HL)_6(Ac)_3(\mu_3\text{-}OH)_9(H_2O)_6]\cdot(ClO_4)_3\cdot 15H_2O$ (Ln^{3+} = Dy^{3+} (**1-*(R/S)***), Y^{3+} (**2-*(R/S)***); H_3L = *(R/S)*-(2-hydroxy-3-methoxybenzyl)-serine)). Strikingly, the comparison of Natural and Magnetic Circular Dichroism (NCD and MCD) and MChD spectra allows an original and unambiguous attribution of the different MChD spectral features observed in these complex systems. The objective is to find design criteria for the preparation of chiral molecular materials highly responsive to MChD.

RESULTS AND DISCUSSION

Synthesis. Compounds **1** and **2** were obtained by reaction of the enantiopure chiral multidentate ligands (*S*)-H_3L and (*R*)-H_3L, prepared by reaction of (*S*)-/(*R*)-serine with *o*-vanilin (Scheme S1), with $Dy(ClO_4)_3$ and $Ni(Ac)_2$ (Ac = acetate) under reflux conditions and controlled pH.

High-resolution electrospray ionization mass spectrometry (HR-ESI-MS), performed starting from both H_2O and MeOH solution, revealed several clear isotope peaks framing a main peak at m/z = 1514.37 for **1** and m/z = 1374.34 for **2**. Following the crystal structure determination presented thereafter, these are assigned to the $[Dy_5Ni_6(HL)_6(Ac)_3(OH)_9(ClO_4)]^{2+}$ and $[Y_5Ni_6(HL)_6(Ac)_3(OH)_9(H_2O)_5(ClO_4)]^{2+}$ species, respectively (Figure S1). All the observed peaks are consistent with the theoretical distributions (Figure S1-S3 and experimental section), and almost all show an intact metal-core frame of the cluster, indicating a remarkably high stability of the self-assembled $\{Ln_5Ni_6\}$ clusters in solution.

Crystal and Molecular Structure. Single crystal X-ray diffraction analysis shows that the four chiral clusters **1-*(R/S)*** and **2-*(R/S)*** are isostructural (Table S1). To illustrate their structural features, herein we discuss in detail only the molecular structure of **1-*(R)***.

1-*(R)* crystallizes in the orthorhombic chiral space group $P2_12_12_1$ and exhibits a cationic cluster core formulated as $[Dy_5Ni_6(S\text{-HL})_6(Ac)_3(\mu_3\text{-OH})_9(H_2O)_6]^{3+}$, three perchlorate counterions, and fifteen water molecules of crystallization (Figure 1).

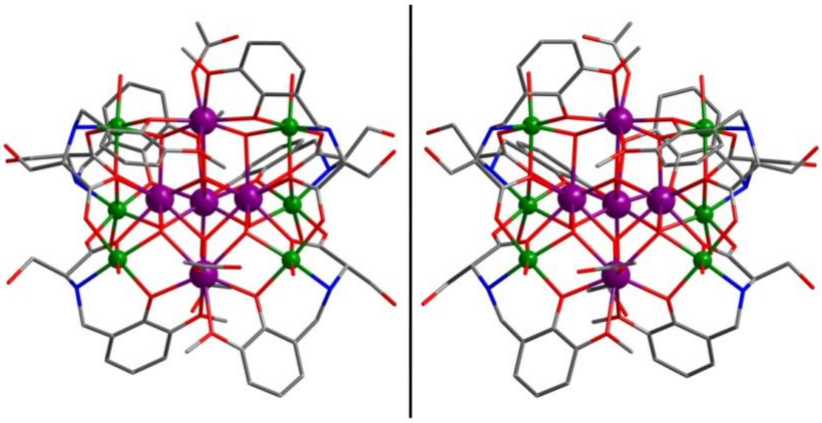

Figure 1. Molecular structures of the $\{Dy_5Ni_6\}$ cluster **1-*(S)*** (left) and **1-*(R)*** (right). Color codes: Ni^{II} green; Dy^{III} purple; O, red; C, gray; N, blue. Perchlorate counterions, water molecules of crystallization and hydrogens are omitted for graphical clarity.

The cationic cluster core contains five Dy^{III} ions, six Ni^{II} ions, nine μ_3-OH^-, six HL^{2-} ligands, three acetate ions and six aqua ligands. The five Dy^{III} ions are linked together by three μ_3-OH^- bonds to form a $[Dy_5(\mu_3\text{-OH})_3]^{12+}$ core featuring a compressed trigonal bipyramidal (TBP) arrangement (Figure 2a and S4), which is rarely reported in *3d-4f* clusters.[40–42] The two Dy^{3+} ions that occupy the axial positions are nonacoordinated and are bridged together by three μ_3-OH^- with a distance of 3.48 Å, which is remarkably shorter than twice of the covalent radius of the metal ions (1.90 Å). The coordination sphere is completed by three additional μ_3-OH^-, each of them bridging an equatorial Dy^{III} and a Ni^{II} ion, and by three carboxylate oxygens (monodentate) of three independent ligands. On the contrary, the three Dy^{3+} ions that occupy the equatorial positions are octacoordinated, and their coordination sphere completed by one μ_3-OH^- bond with the axial Dy^{III} ions, two μ_3-OH^- bonds with an axial Dy^{III} and a Ni^{II} ion, four oxygen atoms of two *o*-vanillin moieties that act in a 1,2-bis-bidentate mode, and one oxygen atom of an acetate ligand.

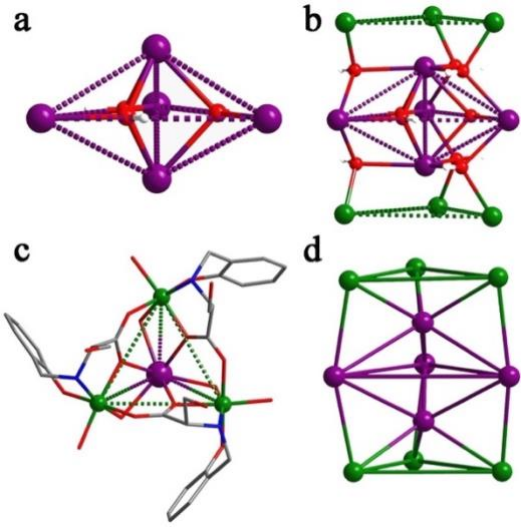

Figure 2. (a) The structure of the TBP $[Dy_5(\mu_3\text{-}OH)_3]^{12+}$ unit; (b) the $[Dy_5Ni_6(\mu_3\text{-}OH)_9]^{18+}$ unit; (c) the Ni_3 triangular unit with terminal ligands; (d) the metal skeleton of $[Dy_5Ni_6]$. Color codes: C, grey; O, red; N, blue; Dy, violet; Ni, green.

Each side edge of the $[Dy_5(\mu_3\text{-}OH)_3]^{12+}$ TBP core is bridged with a Ni^{2+} ion through one μ_3-OH^-. Therefore, the $[Dy_5(\mu_3\text{-}OH)_3]^{12+}$ core and six Ni^{2+} form a $[Dy_5Ni_6(\mu_3\text{-}OH)_9]^{18+}$ metal-hydroxide cluster core (Figure 2b). Two groups of three adjacent Ni^{2+} ions connected by three *syn-anti* carboxylate bridges from three different HL^{2-} ligand (Figure 2c) form a triangular plane that sandwiches the TBP arrangement of the Dy^{III} ions (Figure 2d). Six chiral μ_4-HL^{2-} ligands chelate six Ni^{2+} ions stabilizing and protecting the cluster core (Figure 1). The octahedral coordination geometry around each Ni^{II} ion is completed by an aqua ligand. The Ni–O, Ni–N and Dy–O bond distances in **1-*(R)*** are 2.006(8)–2.118(8) Å, 2.058(11)–2.101(11) Å and 2.235(10)–2.587(9) Å, respectively, which agree well with those reported previously in Ni^{II}–Dy^{III} clusters.[41–43]

Magnetic Properties. The magnetic properties of microcrystalline samples of **1-*(R)*** and ***2*-*(R)***, whose phase purity was checked by powder X-ray diffraction analysis (Figure S5), were investigated in the temperature range 2–300 K under an applied magnetic field $\boldsymbol{B}$ = 0.1 T, and at T = 2 K in the magnetic field range 0.0–7.0 T.

The values of the magnetic susceptibility times the temperature ($\chi_M T$) at room temperature are 78.5 and 7.4 $cm^3\ mol^{-1}$ K, for **1-*(R)*** and **2-*(R)*** respectively (Figure 3), which are in good agreement with the calculated values of 77.8 and 7.2 $cm^3\ mol^{-1}$ K for six uncorrelated Ni^{II} ions (S = 1, g = 2.2) and five uncorrelated Ln^{3+} ions (Dy^{III}, J = 15/2, g = 4/3 (**1**); Y^{III}, diamagnetic (**2**)). As the temperature is decreased from 300 to 20 K, the $\chi_M T$ values for **1-*(R)*** and **2-*(R)*** remain almost constant. Upon further lowering of the temperature, the $\chi_M T$ value of **2-*(R)*** drops

to reach 5.0 cm^3 mol^{-1} K at 2 K, while the $\chi_M T$ value of **1-*(R)*** goes through a little marked minimum before increasing to reach a maximum value of 114.1 cm^3 mol^{-1} K at 2 K.

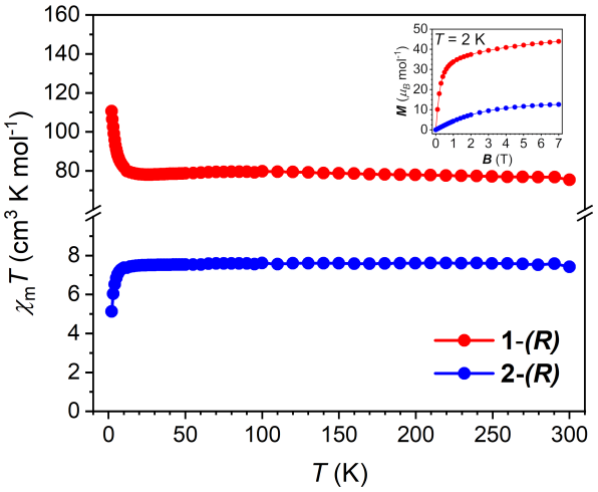

Figure 3. *T* dependence of the $\chi_M T$ at ***B*** = 0.1 T for **1-(*R*)** and **2-(*R*)**. The inset shows the plots of ***M*** vs ***B*** at 2 K.

The behavior observed for compound **2** might arise from the Zero Field Splitting of the Ni^{II} centers and/or antiferromagnetic interactions between them. For **1**, the increase observed at low temperature definitely denotes ferromagnetic interactions between metal ions which rapidly overcome the decrease provoked by Zero Field Splitting and Stark effects in Ni^{II} and Ln^{III} centers, respectively. The complexity of the system precludes the possibility to finely quantify these conflicting phenomena.

The magnetic field dependence of the magnetization of **2-*(R)*** at T = 2 K increases slowly at low magnetic fields, and reaches 12.65 μ_B mol^{-1} at 7.0 T, which is close to the saturation value of 13.2 μ_B mol^{-1} ($M_S = g\ S\ n$; where S = 1, g = 2.2, n = 6) that is expected for a cluster core exclusively based on Ni^{II} paramagnetic ions (Inset of Figure 3). **1-*(R)*** shows instead a magnetization that increases rapidly at low magnetic fields and then reaches 42.37 μ_B mol^{-1} at 7.0 T (Inset of Figure 3). This value is much lower than 63.2 μ_B mol^{-1}, expected assuming $M_S = g\ S\ n + g_J\ J\ m$ (where S = 1, g = 2.2, for n = 6 Ni^{II} centers and J = 15/2, g_J = 4/3, for m = 5 Dy^{III} centers). This is related to a significant single-ion magnetic anisotropy, and it is consistent with the non-superposition of the M versus ***B***/T curves (Figure S6). Indeed, for a sample measured as a microcrystalline powder of randomly oriented crystallites, and assuming a m_J = 15/2 ground state doublet, the equation reported above does not provide a good estimation of the saturation magnetization. M_S = 10 μ_B mol^{-1} is only valid for the molecules having the magnetic anisotropy axis parallel oriented with respect to the magnetic field ***B*** while those oriented perpendicularly to ***B*** provide 0 μ_B mol^{-1}. The powder average for such a system gives

M_S = 5 μ_B mol^{-1}.[44] Considering the coordination environment around the Dy^{III} ions present within our molecular structure, they cannot be considered strongly axial, and this reduces the overall magnetic anisotropy. Assuming an average value of 6.0 μ_B mol^{-1} for each Dy^{III} ion, plus the 13.2 μ_B mol^{-1} contribution of the six Ni^{II} ions (see above) provides a value of M_S of 43.2 μ_B mol^{-1}, in agreement with the experiments. The complexity of the system (Dy^{III} ions in different coordination environments and in different stoichiometric ratio combined with ferromagnetic interactions at low temperature) precludes a finer analysis.

Visible and Near Infrared Light Absorption. The absorption properties of **1-*(R)*** and **2-*(S)*** were investigated on oriented single crystals in the 420–1000 nm range for temperatures going from 290 to 4 K (Figure 4). The measurements were performed in transmission mode with the light wavevector ***k*** aligned parallel to the *c* crystallographic axis.

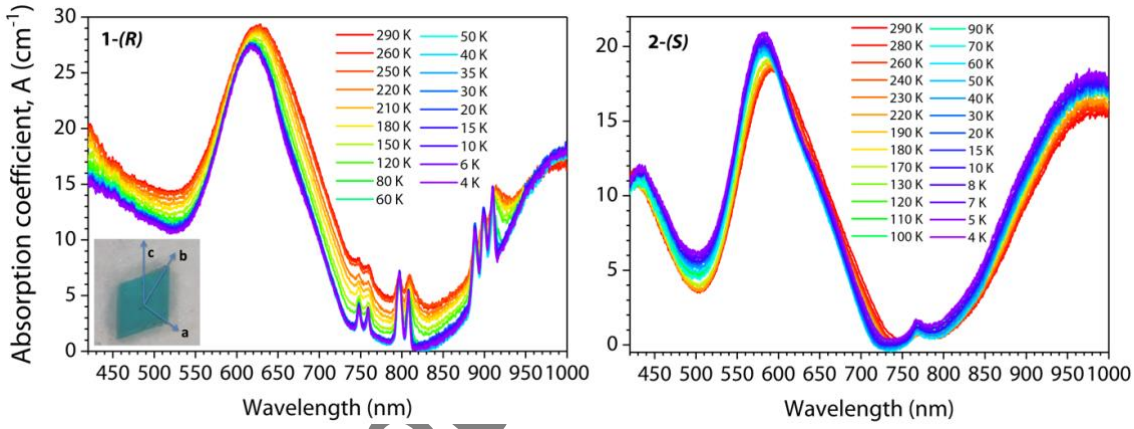

Figure 4. Temperature dependence of the Vis-NIR absorption spectra (420-1000 nm) of a single crystal of **1-*(R)*** (left) and **2-*(S)*** (right). Inset shows a typical indexed single crystal of **1**.

At room temperature, the electronic spectra of **1-*(R)*** and **2-*(S)*** show a common feature: two intense absorptions centered at ca. 600 and 1000 nm. In view of their energy, high absorption coefficient and their presence in both **1** and **2** with only a minor shift in the position of their maxima, these absorptions are assigned to the $^3T_1 \leftarrow {}^3A_2$ and $^3T_2 \leftarrow {}^3A_2$ spin-allowed electronic transitions of the octahedrally coordinated Ni^{II} sites, respectively (the ground state term is ^3F).[20,45,46] **2-*(S)*** shows an additional band with a much lower absorption coefficient at ca. 770 nm. In view of its energy and low absorption coefficient, this band, which is not well visible in **1-*(R)*** as other bands are present in the same spectral range (*see below*), is assigned to the $^1E \leftarrow {}^3A_2$ spin-forbidden electronic transition of the Ni^{II} sites.[20,45,46] **1-*(R)*** shows three additional groups of multiple absorption bands characterized by low absorption coefficients at ca. 750, 800 and 900 nm. By lowering the temperature down to 4 K, these bands became well defined, evidencing their intrinsic sharp nature, their precise number and their intensity. These

features point out that these bands are clearly associated to *f-f* electronic transitions of the Dy^{III} sites, its ground state spectroscopic level being $^6H_{15/2}$. Because the energy of *f-f* transitions is only slightly affected by ligand field effects, these bands can be assigned on the basis of their energy as follows: the two absorption bands centered at ca. 750 nm are assigned to the $^6F_{3/2} \leftarrow {}^6H_{15/2}$ transition, the two absorption bands centered at ca. 800 nm are assigned to the $^6F_{5/2} \leftarrow {}^6H_{15/2}$ transition and the three absorption bands centered at ca. 900 nm to the $^6F_{7/2}/{}^5H_{5/2} \leftarrow {}^6H_{15/2}$ transition, which involves a mixing of the $^6F_{7/2}$ and $^5H_{5/2}$ excited states.[47–53] The temperature lowering does not affect remarkably the absorption bands assigned to the Ni^{II} sites, with only a clear blueshift of ca. 20 nm observed for the band associated to the $^1T_1 \leftarrow {}^3A_2$ for both **1** and **2**, most probably due to the depletion of the vibrational levels of the ground state upon temperature lowering.

By taking advantage of the stability of the $\{Ln_5Ni_6\}$ clusters in solution demonstrated by HR-ESI-MS, optical studies in methanol at room temperature have been performed. This was done for two reasons: first, to extend the investigation of the absorption properties in the Near Infrared range up to 1400 nm; second, to have access to the natural circular dichroism (NCD) and magnetic circular dichroism (MCD) spectra of compounds **1** and **2**. Indeed, these data are much more easily obtained working in diluted liquid solution than in the solid-state or in frozen-solutions. These measurements in solution provide an isotropic circular dichroic response, representative of all possible orientations of the molecules with respect to the circularly polarized light wavevector, while working on oriented systems in the solid state provides information on the intrinsic anisotropic circular dichroism.[54] Furthermore, irradiation of oriented systems in the solid state with circular polarized light might results in linear birefringence and dichroism that can interfere with the circular dichroic response. These different contributions can be revealed and isolated by specific procedures, such as a collection of spectra by rotating the sample around the optical axis, but this requires adapted experimental setups.[55]

The absorption spectra recorded in H_2O and in MeOH solution show for both enantiomers the same spectral features and the same absorption bands observed in the solid state (Figures S7 and S8). **1** does not show any variation in the positions of the maxima passing from solid-state to solution, regardeless the solvent, while **2** shows a redshift of ca. 30 nm for the Ni^{II} spin-allowed transitions and a blueshift of ca. 20 nm for the spin-forbidden band, independently on the solvent used. Interestingly, by extending the investigation up to 1360 nm, we are able to identify additional groups of sharp bands at ca. 1100 and 1280 nm for **1**, that are superimposed

on the broad low energy absorption of the Ni^{II}. These transitions, that are better resolved when investigating the magnetic circular dichroism (MCD) and MChD spectra (*see below*), are assigned to the $^6F_{9/2}/^5H_{7/2} \leftarrow {}^6H_{15/2}$ and $^6F_{11/2}/^5H_{9/2} \leftarrow {}^6H_{15/2}$ transitions of the Dy^{III} sites, respectively.[47–53] Another absorption split in two components and superimposed on a broad and intense high energy absorption is observed at ca. 450 nm. This is assigned to the $^4F_{9/2} \leftarrow {}^6H_{15/2}$ of the Dy^{III} sites (Figures S7 and S8).[47–53]

Natural Circular Dichroism. The NCD spectra of **1-*(R/S)*** and **2-*(R/S)*** in MeOH solution were investigated to get insights into the chiroptical properties of these chiral clusters. As shown in Figure 5a, the NCD spectra of **1** and **2** are essentially superimposable, with two main signals centered at ca. 670 nm and ca. 1190 nm, the latter accompanied by a shoulder of weak intensity at ca. 940 nm. These contributions to the NCD spectrum are ascribed to the $^3T_1 \leftarrow {}^3A_2$ and $^3T_2 \leftarrow {}^3A_2$ transitions of the octahedrally coordinated Ni^{II} sites, respectively, the latter composed of two contributions: $^3A_1 \leftarrow {}^3A_2$ and $^3E \leftarrow {}^3A_2$.[20,45,46] The relative position, intensity, splitting and broadness of the NCD signals are in agreement with what was already observed for other chiral Ni^{II}-based octahedrally coordinated complexes.[20,45,46] The perfect mirror-symmetry of the NCD spectra for the two enantiomers confirms the enantiomeric properties of **1-*(R/S)*** and **2-*(R/S)***, indicating that the chirality is successfully transferred from the ligand to the metal centers. On the contrary, the electronic transitions associated to the Dy^{III} ions observed for compound **1** do not contribute to the NCD spectra, which is totally dominated by the Ni^{II} contributions. This might be correlated to the weaker absorption of the lanthanide centers and/or a lesser influence of the chiral ligands, but also a direct consequence of the intrinsically low rotary strength of these transitions. Indeed, none of them are classified as "CD-sensitive" according to the Richardson's optical activity selection rules.[56]

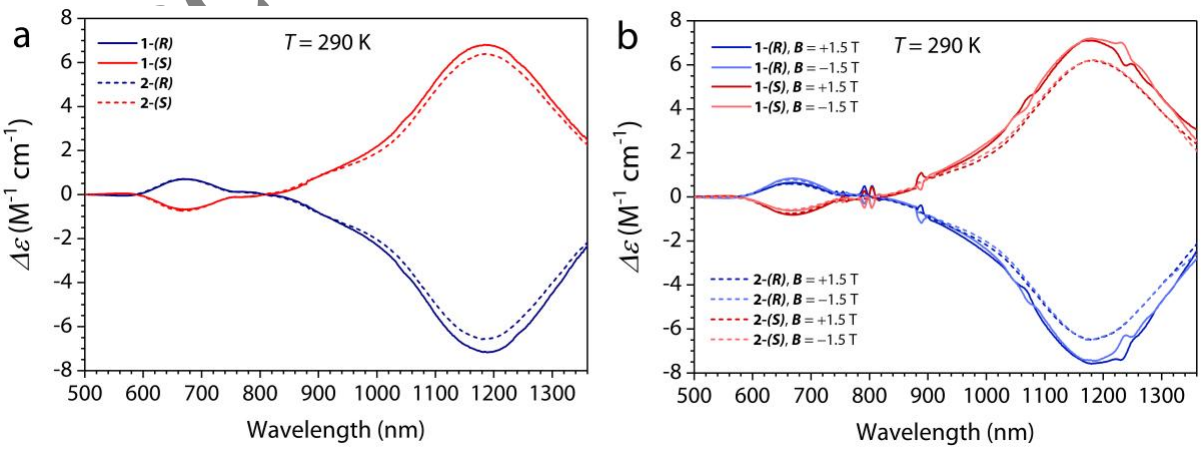

Figure 5. Room temperature NCD spectra (500-1360 nm) of **1-*(R/S)*** and **2-*(R/S)*** (see legend) in MeOH solution at $\boldsymbol{B}$ = 0 T (a) and at $\boldsymbol{B}$ = ±1.5 T (b).

Overall, this highlights the higher NCD response of the Ni^{II} sites as compared to the NCD response of the Dy^{III} sites. This emerges more clearly when the same measurements are performed under an externally applied magnetic field $\boldsymbol{B}$ = ±1.5 T. As shown in Figure 5b, the NCD spectrum of **2-*(R/S)*** under magnetic field is basically the same collected at $\boldsymbol{B}$ = 0 T, while that of **1-*(R/S)*** show additional signals at the same wavelengths of the absorption bands revealed through absorption spectroscopy in the solid state and in solution.

Magnetic Circular Dichroism. The MCD spectra, obtained as MCD = [NCD(+1.5 T) – NCD(–1.5 T)]/2,[57,58] indeed show significant differences between **1-*(R/S)*** and **2-*(R/S)*** (Figure 6). **2-*(R/S)*** shows weak and broad MCD signals associated to the Ni^{II} transitions. In **1-*(R/S)*** these two contributions are still present but accompanied by additional sharp signals associated to the *f-f* transitions of the Dy^{III} sites. These MCD bands appears particularly sharp for the highest energies and became broader as the energy is reduced. However this broadness is essentially a consequence of the fact that the spectrum has been plotted, for practical reasons (comparison with Absorption and NCD spectra), as a function of the wavelength instead of the frequency of the incident radiation. Indeed, when plotted versus frequency (Figure S9) the different MCD signals show an almost constant bandwidth (Table S2).

Overall, the MCD highlights a stronger response of the Dy^{III} sites to the magnetic field as compared to the Ni^{II} sites.

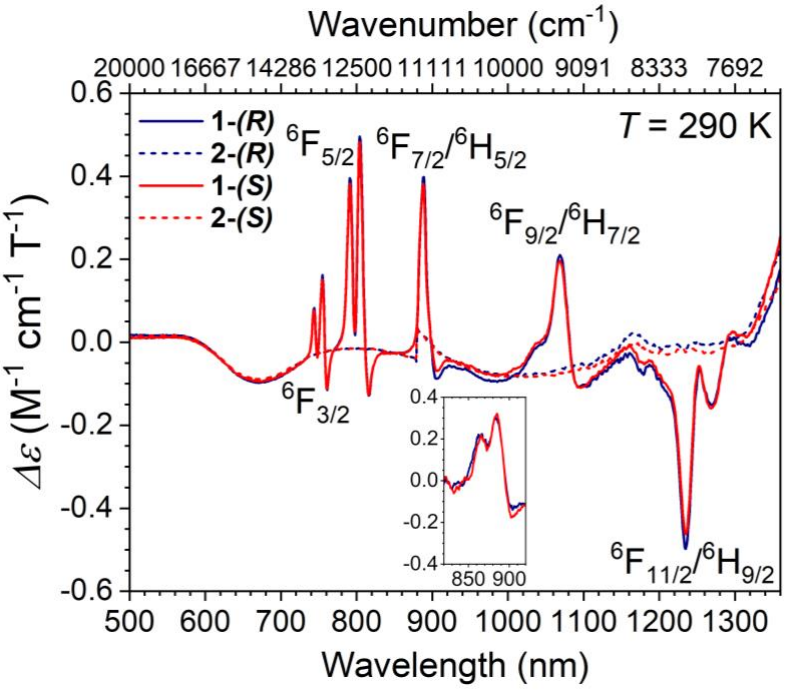

Figure 6. Room temperature MCD spectra (500-1360 nm) of **1-*(R/S)*** and **2-*(R/S)*** (see legend) in MeOH solution. Inset show the real shape of the signal at ca. 900 nm in the main figure that is affected by the change of detector (see experimental section).

The relative intensity of the MCD signals follows the intensity of the originating absorption bands, thus seems mainly driven by the intrinsic transition probability of the electronic transition themselves. However, the number and the shape of the MCD bands for each electronic transition deserve further comments. All of them have a similar shape, with two contributions of the same sign at high energy and one contribution of opposite sign at low energy. This is also the case for the transition at ca. 900 nm (see inset and details in the experimental section). These features are less evident for the two lowest energy transitions. One can wonder if their fine structure is due to a crystal field splitting of the originating electronic transition whose main energy is dictated by spin-orbit coupling, as commonly observed for lanthanides, or by the different coordination environments of the Dy^{III} sites that are present in the chiral clusters **1-*(R/S)***. To probe these two possibilities, we focused on the MCD signals related to the two electronic transitions that are associated to pure excited states, which are the best defined, $^6F_{3/2} \leftarrow {}^6H_{15/2}$ and $^6F_{5/2} \leftarrow {}^6H_{15/2}$. If the crystal field splitting of the excited state in $(2J+1)/2$ Kramers doublets is taken into account, the $^6F_{3/2}$ state is expected to provide two sublevels, while the $^6F_{5/2}$ state provides three sublevels. Such a difference is expected to modify the overall shape of the signal as a different number of transitions are allowed, instead, the shape is very similar. Furthermore, typical MCD signals for mononuclear Dy^{III} complexes do not show such splitting,[47–53] thus indicating that the presence of Dy^{III} sites in two crystallographically inequivalent environments can be the reason of such a spectral feature.

To better probe this possibility, we have analysed the MCD signals associated to the $^6F_{3/2} \leftarrow {}^6H_{15/2}$ and $^6F_{5/2} \leftarrow {}^6H_{15/2}$ transitions by a multiple regression fit analysis. Two contributions to the MCD signal are expected.[55,59,60] The A term, which is associated to the lifting of degeneracy of ground and excited state levels due to the magnetic field (Zeeman splitting). It is temperature independent and has a derivative-shape signal. The C term, which is associated to a different population of the ground state as a function of the temperature (Boltzmann distribution). It varies as $1/T$ and has an absorption-like band shape.[55,59,60] At room temperature one can expect that both C and A terms contribute to the MCD signal for a paramagnetic ion, whereas the C term dominates at low temperature.ref In the experimental spectra recorded at room temperature one can indeed recognized that both contributions are present. A multiple regression fit of $^6F_{3/2}$ and $^6F_{5/2}$ multiplets that take into consideration both C and A terms was performed to quantify these contributions.[38] This procedure reproduces the experimental data well (Figure S10 and Experimental Section for details). Furthermore, the ratio between the intensity of the C terms contributions within the $^6F_{5/2}$ and $^6F_{3/2}$ multiplets, are ca. 0.65 and ca. 0.71, respectively, that are, within the experimental accuracy, close to 0.66, the 2:3

stoichiometry ratio between the crystallographically inequivalent Dy^{III} ions present in the molecular structure. The slight overall shift between the energy of the entire series of *f-f* transitions for the two crystallographically independent Dy^{III} ions is justified by the crystal field effects (different coordination environment) that contribute by slightly changing the energy difference between the ground state $^6H_{15/2}$ and the excited states for the two ions, while remaining mainly determined by the intrinsic spin-orbit coupling constant of the lanthanide ion (*see above*).[47–53]

Magneto-Chiral Dichroism. MChD measurements were performed in the temperature range T = 4−150 K with an alternating (Ω = 1.5 Hz) magnetic field $\boldsymbol{B}$ = ±0.860 T applied along the wavevector $\boldsymbol{k}$ on the same oriented crystals used for the collection of the absorption spectra in the solid state. The MChD spectra at T = 4 K of the two enantiomers of **2** are shown in Figure S11. The MChD spectra can be rationalized as follows. The absence of paramagnetic *4f* ions in the molecular structure leads to MChD signals that are clearly associated to the Ni^{II} ions, in agreement with the absorption spectrum and the NCD and MCD responses. Three main MChD signals are observed. The signals at 560 and 1050 nm are associated to the $^3T_1 \leftarrow {}^3A_2$ and $^3T_2 \leftarrow {}^3A_2$ transitions. The sharper signal at ca. 770 nm is instead associated to the $^1E \leftarrow {}^3A_2$ spin-forbidden electronic transition. The temperature dependence of the MChD spectrum for the **2-*(S)*** enantiomer (4–150 K) (Figure S12) shows a decrease in intensity for all signals as the temperature increases, with ΔA_{MChD} values in agreement with the temperature dependence of its magnetization measured with the same applied magnetic field (Figure S13).[24,38,61]

Figure S14 shows the MChD spectra for the two enantiomers of **1** at T = 4 K while the temperature dependence in the full range is shown in Figure 7 for **1-*(R)***.

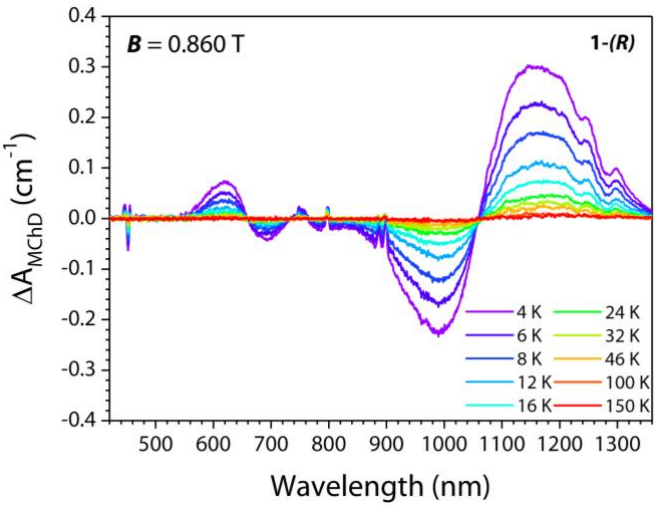

Figure 7. Temperature variation (see legend) of MChD spectra (420-1360 nm) of **1-*(R)*** recorded on an oriented single crystal under an applied magnetic field $\boldsymbol{B}$ = ±0.860 T.

The MChD spectra are extremely rich with intense MChD signals observed all along the investigated spectral range. On the basis of the assignment of the electronic transitions performed analysing the absorption, NCD and MCD spectra, the MChD contributions can be easily attributed. Going from high to low energy one can identify a sharp negative absorption-like MChD signal at ca. 450 nm associated to the $^4F_{9/2} \leftarrow {}^6H_{15/2}$ (Dy^{III}) transition, a derivative-type broader signal at ca. 650 nm associated to the $^3T_1 \leftarrow {}^3A_2$ (Ni^{II}) transition, a weak signal at ca. 750 nm associated to the $^6F_{3/2} \leftarrow {}^6H_{15/2}$ (Dy^{III}) transition, a sharp absorption-like signal at ca. 800 nm associated to the $^6F_{5/2} \leftarrow {}^6H_{15/2}$ (Dy^{III}) transition and two sharp absorption-like signals at ca. 900 nm associated to the $^6F_{7/2}/{}^5H_{5/2} \leftarrow {}^6H_{15/2}$ (Dy^{III}) transition. Then, a broad signal of overall derivative-type shape centered at ca. 1060 nm and associated to the $^3T_2 \leftarrow {}^3A_2$ (Ni^{II}) transition is observed. This broadness hampers the observation of a MChD signal for the $^6F_{9/2}/{}^5H_{7/2} \leftarrow {}^6H_{15/2}$ (Dy^{III}) centered at ca. 1080 nm, but allows the observation of additional MChD signals at ca. 1250 nm that are associated to the $^6F_{11/2}/{}^5H_{9/2} \leftarrow {}^6H_{15/2}$ (Dy^{III}) transition. By increasing the temperature, the overall MChD spectrum loses intensity to reach values of ΔA_{MChD} that are comparable to the background only when the temperature reaches 150 K. This is not surprising given the proportionality of ΔA_{MChD} with the magnetization of the system, that follows the Curie law (proportionality with $1/T$) in most of the investigated T range and the dominance of the C term.[20,38]

All the identified Ni^{II} and Dy^{III} electronic transitions provide multi-metal site MChD signals with a significant intensity, although the intensities of Dy^{III} signals are not as intense as it might be expected if one considers the intrinsically high single-ion magnetic anisotropy of this lanthanide ion due to its electronic configuration. At the same time, the reduced influence of the chiral ligands on the coordination geometry of the Dy^{III} centres compared to the Ni^{II} ions might have an effect on this regard and needs further investigations.

To quantitative estimate the portion of the absorption that is affected by the interaction of the chiral system with the magnetic field with respect to the overall absorption, we have calculated the g_{MChD} values for those transitions that are not superposed with other ones. These provides values of g_{MChD} of 0.016 T^{-1} and 0.020 T^{-1} for the electronic transitions at ca. 810 and 910 nm, respectively, which are in the average range among the g_{MChD} values reported so far in the literature.[7,8,21,25,61]

MChD measurements were also performed as a function of the magnetic field $\boldsymbol{B}$ (0.0−1.50 T range) at T = 5.0 K. Figure 8 shows the magnetic field dependence of the MChD spectra for **1-*(R)*** in the 400−750 nm range. This range was selected because it provides information about

the intensity of one Dy^{III} electronic transition and one Ni^{II} electronic transition without superposition with other bands.

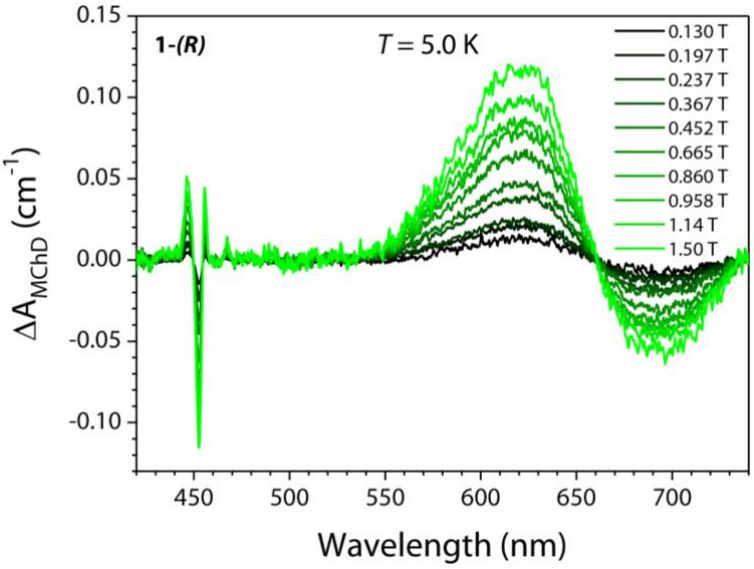

Figure 8. Magnetic field variation (see legend) of MChD spectra (420-1360 nm) of **1-*(R)*** recorded on an oriented single crystal under at T = 5 K.

The intensity of the MChD signals increase linearly as the intensity of the magnetic field increases without reaching saturation at 1.5 T. Figure 9 shows a comparison between the temperature and magnetic field dependence of the absolute values of ΔA_{MChD} and the magnetization of the sample measured in the same conditions ($\boldsymbol{B}$ = 0.860 T, T = 5 K). The magneto-chiral optical data reproduce the dependence of the magnetization both as a function of the temperature and the magnetic field well, but more importantly, any remarkable difference is observed between the signals associated to Ni^{II} and Dy^{III}. This is in agreement with the MChD theory but it is different with what was previously observed with hard X-rays in a *3d-4f* heterometallic chiral complex investigated at room temperature. Indeed, only a MChD signal associated to the X-rays absorption of the Tb^{III} ion was observed, while the Ni^{II} absorption did not provided any observable MChD signal.[22] Here we show that in a heterometallic cluster having two magnetic sites potentially able to provide a MChD signal on the basis of their NCD and MCD response, at a given temperature and at a given value of the applied magnetic field, the normalized intensity of their MChD signals is, within the experimental accuracy, the same.

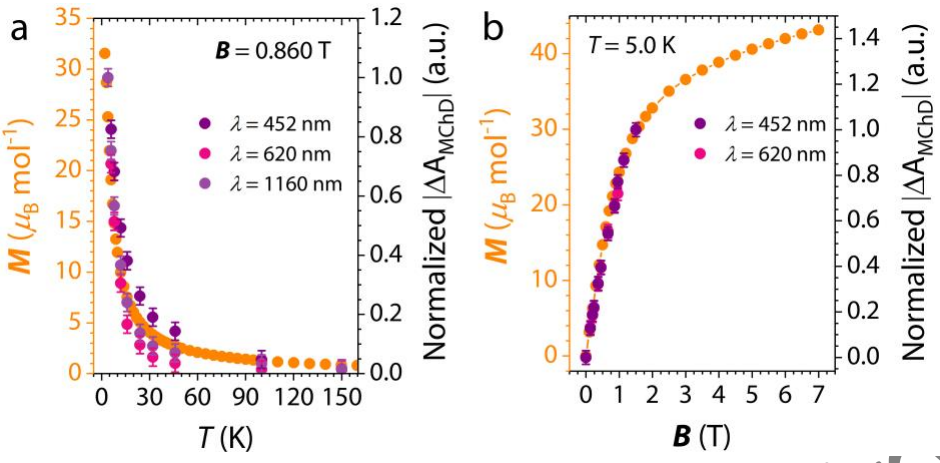

Figure 9. Temperature (a) and magnetic field (b) dependence of ΔA_{MChD} signals (see legends) of **1-*(R)*** compared to magnetization data.

Thus, signals associated to multiple sites are perfectly distinguishable and, although the origin of the MChD signal appear to be dictated by different phenomena, NOA for Ni^{II} and MOA for Dy^{III}, a synergy between the optical response of the different metal sites is observed. This is correlated to the dependence that MChD has with the magnetization of the sample. Here, the high value of the overall magnetization generated by a complex molecular structure able to gather together five Dy^{III} ions and six Ni^{II} ions, allows the MChD signals of both *3d* and *4f* ions to be detected up to 150 K. Detectable MChD at such temperatures are not easily accessible for single isolated paramagnetic ion in mononuclear complexes with a low magnetization and a *T* dependence that strictly follows the Curie law, thus evidencing the fundamental role of the chiral multimetallic cluster.

It should be however noted that the absorption bands associated to the Dy^{III} ions do not provide MChD signals of the same intensity. By restricting the attention to the spectral region where no superposition with Ni^{II} bands is present, between 720 and 850 nm, we can clearly see that the two absorptions at ca. 800 nm, that have been assigned to Dy^{III} sites having different coordination environments (*see above*) do not contribute equally to the MChD spectrum. Indeed, only one intense contribution at 810 nm is observed, which is associated to the three Dy^{III} ions that occupy external positions in the TBP cluster. This is not surprising as it has been already observed in a previous study that when multi-metallic systems are concerned, the metal ions bonded by the chiral ligands are those that provide the most intense MChD signals.[24] Here the external Dy^{III} ions are indeed coordinated by two chiral ligands, each of them acting in a bidentate mode, while the internal ones are coordinated only by two terminal carboxylate oxygens in a monodentate mode, with the rest of the coordination geometry completed by hydroxido ligands.

CONCLUSIONS

In conclusion, 3*d*-4*f* $\{Ln_5Ni_6\}$ (Ln = Dy^{III}, Y^{III}) enantiopure chiral clusters were synthesized through a self-assembly process leading to heterometallic complexes that are highly stable in solution and in the solid state. Single-Crystal X-ray diffraction revealed that the metal ions are held together by μ_3-OH^- bridges leading to clusters where the six Ni^{2+} ions and the five Ln^{3+} ions organize into a structure featuring two outer Ni_3 triangles sandwiching a Ln_5 trigonal bipyramid. Both metal ions interact with the chiral ligands that prevent the cluster from further growth. The hydroxide bridges mediate antiferromagnetic interaction between Ni^{II} ions and ferromagnetic interaction between Ni^{II} and Dy^{III} ions.

A thorough spectroscopic study of the optical, magneto-optical and magneto-chiral optical properties evidences that in the Vis-NIR range, the Natural Circular Dichroism is dominated by the *3d* ions whereas the Magnetic Circular Dichroism by the *4f* ions. The Magneto-Chiral Dichroism resulting from the interplay between the two former phenomena appeared as a combination of signals driven by the Natural Optical Activity of the *3d* ions and the Magnetic Optical Activity of the *4f* ions. This defines a chemical strategy for designing optically active SMMs for the optical readout of magnetic data. One can indeed rely on MChD-active polymetallic chiral clusters containing both *3d* and *4f* ions, selecting transition metals whose *d-d* transitions have a high NOA and anisotropic lanthanide ions featuring *f-f* transitions with a high MOA. The objective is to have strong enough MChD signals to read-out the magnetization stored in a single molecule with a simple and undamaging unpolarized light (Vis-NIR). To achieve this, chiral SMMs with opened hysteresis cycles, that are, to date, extremely rare, have to be synthetized. This works provides design criteria towards this direction.

EXPERIMENTAL SECTION

General Remarks. All of the chemicals were purchased from commercial sources and used as received. Aqueous solutions of lanthanide perchlorates (1 mol L^{-1}) were prepared by digesting lanthanide oxides in concentrated perchloric acid with great care.

Caution! Although not encountered in our experiments, perchlorate salts in the presence of organic ligands are potentially explosive. Only a small amount of the materials should be prepared and handled with care.

Synthesis of N-(2-hydroxy-3-methoxybenzyl)-L/D-serine (S/R-H_3L): *(S)*-H_3L was synthesized according to the literature,[62] but the procedure was slightly modified. To a solution of 1.576 g of *L*-serine (15 mmol) and 0.600 g of NaOH (15 mmol) in 60 mL of a methanol:water mixture

(v/v 1:1) was added 2.834 g (15 mmol) of *o*-vanillin. The resulting yellow solution was stirred for five hours at room temperature. 0.567 g of $NaBH_4$ (15 mmol) was added to it at 0 °C and the solution was stirred until the yellow color disappeared. The pH of the solution was adjusted to 5 using ~ 6mL of glacial acetic acid and stirred for half an hour. A white precipitate thus formed was filtered off, washed with methanol and air dried. Yield: 2.6 g (59%). *(R)*-H_3L was prepared following the procedure described for *(S)*-H_3L except that 1.576 mg (15 mmol) of *D*-serine was used instead of *L*-serine.

Synthesis of [Dy$_5$Ni$_6$(S/R-HL)$_6$(Ac)$_3$(μ$_3$-OH)$_9$(H$_2$O)$_6$]·(ClO$_4$)$_3$·15H$_2$O (1-(R/S)): *(S)*-H_3L or *(R)*-H_3L (0.06 g, 0.25 mmol), $Ni(Ac)_2$ (0.5 mol L^{-1},1.5 mL), $Dy(ClO_4)_3$ (1.0 mol L^{-1},1.25 mL) was added to 10 mL deionized water. The resulting solution was heated to about 80 °C and a freshly prepared NaOH solution (aq. 0.5 mol L^{-1}) was added dropwise to the point of incipient but permanent precipitation (pH ≈ 6.4), the solution was refluxed for 2 hours and then filtered. Evaporation of the filtrate under ambient conditions afforded 0.22 g grassy rhombic crystals after one day. (Yield are 37% and 36% for **1-*(R/S)*** based on $Dy(ClO_4)_3$. HR-MS (ESI) m/z: calcd. for **1-*(R/S)***, $[Dy_5Ni_6(HL)_6(OH)_9(AC)_4]^{2+}$ 1494.75, $[Dy_5Ni_6(HL)_6(OH)_9(AC)_3(ClO_4)]^{2+}$ 1514.97, $[Dy_5Ni_6(HL)_6(OH)_9(AC)_2(ClO_4)_2]^{2+}$ 1535.2, $[Dy_5Ni_6(HL)_6(OH)_9(AC)(ClO_4)_3]^{2+}$ 1555.4, $[Dy_5Ni_6(HL)_6(OH)_9\ (ClO_4)_4]^{2+}$ 1575.65; found, 1494.4, 1514.37, 1534.83, 1554.8 and 1575.27. Anal. calcd for **1-*(R/S)*** (FW = 3606.99): C, 23.94; H, 3.82; N, 2.33. Found: C, 23.94; H, 3.37; N, 2.35.

Synthesis of [Y$_5$Ni$_6$(S/R-HL)$_6$(Ac)$_3$(μ$_3$-OH)$_9$(H$_2$O)$_6$]·(ClO$_4$)$_3$·15H$_2$O (2-(R/S)): **2-*(R/S)*** were synthesized in a similar fashion as **1-*(R)/(S)***, except different $Y(ClO_4)_3$ was used instead of $Dy(ClO_4)_3$. Yield is 35% for **2-*(R/S)*** based on $Dy(ClO4)_3$. HR-MS (ESI) m/z: calcd. for **2-*(R/S)***, $\{[Y_5Ni_6(HL)_6(Ac)_3(OH)_9(H_2O)_6]^{3+}\cdot ClO_4^-\cdot HAc\cdot 3H_2O\}^{2+}$ 1440.876, $\{[Y_5Ni_6(HL)_6(Ac)_3(OH)_9(H_2O)_6]^{3+}\cdot ClO_4^-\cdot HAc\}^{2+}$ 1413.860, $\{[Y_5Ni_6(HL)_6(Ac)_3(OH)_9(H_2O)_5]^{3+}\cdot ClO_4^-\}^{2+}$ 1374.845, $\{[Y_5Ni_6(HL)_6(Ac)_3(OH)_9(H_2O)_2]^{3+}\cdot ClO_4^-\}^{2+}$ 1347.808, $\{[Y_5Ni_6(HL)_5L(Ac)_2(OH)_9(H_2O)]^{3+}\cdot ClO_4^-\}^{2+}$1308.802, $\{[Y_5Ni_6(HL)_3L_3(Ac)_2(OH)_7]^{3+}\cdot ClO_4^-\}^{2+}$ 1281.808, $\{[Y_5Ni_6(HL)_6(Ac)_3(OH)_9(H_2O)_6]^{3+}\cdot 3HAc\cdot HClO_4\cdot 7H_2O\}^{3+}$ 1024.935, $\{[Y_5Ni_6(HL)_6(Ac)_3(OH)_9(H_2O)_6]^{3+}\cdot\cdot 2HAc\cdot 7H_2O\}^{3+}$ 971.608, and $\{[Y_5Ni_6(HL)_6(Ac)_3(OH)_9(H_2O)_6]^{3+}\cdot Hac\cdot 6H_2O\}^{3+}$ 945.623; found, 1440.905, 1413.957, 1374.870, 1347.901, 1308.818, 1281.860, 1025.037, 971.669, 945.621. Anal. calcd. for **2-*(R/S)*** (FW = 3239.04): C, 26.68; H, 4.26; N, 2.59. Found: C, 26.58; H, 3.88; N, 2.62.

Characterization. The C, H, and N microanalyses were carried out with a CE instruments EA 1110 elemental analyzer. The infrared spectra (IR) were recorded on a Nicolet AVATAR FT-IR 380 Spectrophotometer with pressed KBr pellets.

High-resolution Electrospray Ionization Mass Spectrometry. The high-resolution electrospray ionization mass spectrometry (HRESI-MS) data were collected on Bruker En Apex ultra 7.0 T FT-MS and the data processed using the Bruker Daltonics Data Analysis 3.3 software, while simulated isotope patterns were investigated using Bruker Isotope Pattern software.

X-Ray Crystallography. Single crystal X–ray structure determination on compounds **1-*(R/S)*** and **2-*(R/S)*** were collected on an Oxford Gemini S Ultra CCD area detector with monochromatic Mo Kα radiation (λ = 0.71073 Å) at 173 K. Absorption corrections were applied by using the multi-scan program CrysAlis Red. The structures were solved by direct methods, and non-hydrogen atoms were refined anisotropically by least-squares on F2using the SHELXTL–97 program.[63] The hydrogen atoms of the organic ligand were generated geometrically (C–H, 0.96 Å). Crystal data as well as details of data collection and refinement for the complexes are summarized in Table S1. CCDC 2125546-2125549 contains the supplementary crystallographic data for this paper. These data can be obtained free of charge from The Cambridge Crystallographic Data Centre via www.ccdc.cam.ac.uk/data_request/cif. X-ray powder diffraction studies (PXRD) were performed using a Rigaku Ultima IV diffractometer with Cu-Kα radiation (λ = 0.15418 nm, 35.0 kV, 15.0 mA). The calculated PXRD patterns were generated from single crystal reflection data using Mercury 3.7.[64]

Magnetic measurements. Magnetic measurements were carried out with a Quantum Design SQUID MPMS magnetometer working in the 2-300 K range. Diamagnetic corrections were made with Pascal's constants.[65]

Circular and Magnetic Circular Dichroism Spectroscopy. The circular dichroism (CD) and magnetic circular dichroism (MCD) spectra were recorded using a Circular Dichroism Spectrometer, model: Chirascan Plus, Applied Photophysics Ltd, UK. The magnet was put into the sample cell under two conditions: 1) the magnetic direction was parallel with the polarized light (NS); 2) the magnetic direction was antiparallel with the polarized light (SN). The final MCD signals were introduced as (NS-SN)/2. The high-resolution spectra reported in the main figure were obtained superposing two acquisition with different detectors that are sensitive to UV-Vis and NIR light, respectively. However, both have a poor sensitivity at ca. 900 nm. The

result is a signal that has only two contributions of different intensity and opposite signs. If the data collection is performed on the same sample with another detector that has an overall lower resolution but do not lose sensitivity around 900 nm, a signal with a shape very similar to the other signals is obtained (inset in Figure 6). The multiple regression fit used to analyse the $^6F_{5/2}$ and $^6F_{3/2}$ multiplets have been performed as follows: a gaussian curve with a fwhm (130 cm^{-1}) comparable to that of the positive signal centered at ca. 12430 cm^{-1} has been taken as a reference for the C-terms and the A-term obtained by calculating the first derivative of this curve. The position of these curves has been adjusted on the basis of the experimental spectrum and two identical C-term and A-term curves have been used to fit the second component of the $^6F_{5/2}$ multiplet. The same was done for the $^6F_{3/2}$ multiplet starting from a gaussian function with a smaller fwhm (100 cm^{-1}). Therefore, the frequency and the fwhm of all curves was kept fix and the only parameters that were free to vary are the coefficients of the multiple-regression fit that define the intensity of the various contributions. The overall Adj-R^2 was 0.9685 and the coefficients of the regression fit and their standard errors reported in Table S3.

Magneto-Chiral Dichroism Spectroscopy. MChD spectra were recorded with a home-made multichannel MChD spectrometer operating in the visible and near infrared spectral window (420–1360 nm) between 4.0 and 300 K with an alternating magnetic field $\boldsymbol{B}$ up to ±2 T. A detailed description of the measurement apparatus has been reported elsewhere.[66] MChD spectra were acquired on single crystals of enantiopure **1-*(R/S)*** and **2-*(R/S)***. The samples were mounted on a titanium sample holder over a 0.8 mm hole diameter centered with respect to a 1.0 mm diameter collimated beam. Measurements were performed in the 4.0–150 K range with an alternating magnetic field $\boldsymbol{B}$ = ±1.0 T and frequency Ω = 0.04 Hz. MChD spectra as a function of the magnetic field were recorded at T = 4.0 K for alternating magnetic fields of different amplitudes (0.0-1.50 T). The MChD signals were obtained at each temperature/field by recording, on average, 30.000 spectra with an integration time, t_{int} of 5 ms, every 10 ms. Unpolarized light was provided by Thorlabs broadband Tungsten-Halogen (Thorlabs SLS201L) for wide-range Vis-NIR measurements. The data were collected with a OPTOSKY detector equipped with a thermoelectric cooled sensor operating in the 420–1000 nm spectral region with a resolution of 16 bits. Each spectrum was correlated to a specific magnetic field value by a dual channel digitizer (Picoscope 5000B) acquiring simultaneously triggers from the spectrometer and the magnetic field from a Hall effect sensor placed in proximity of the sample. Data are then post-processed as a synchronous detection with a MatLab routine to obtain a MChD spectrum. The g_{MChD} value is obtained by using the following equation:

$$g_{\mathrm{MChD}} = 2\frac{\Delta A_{\mathrm{MChD}}}{A}$$

$g_{MChD} = 2\Delta A/A$ if $\Delta A_{MChD} \equiv (A(\boldsymbol{B} \neq 0)–(A(\boldsymbol{B} = 0))$ or $\Delta A/A$ if $\Delta A_{MChD} \equiv (A(\boldsymbol{B}\uparrow)–(A(\boldsymbol{B}\downarrow))$. Our data treatment software calculates ΔA_{MChD} as $A(\boldsymbol{B} \neq 0)–A(\boldsymbol{B} = 0)$, and the effective absorption coefficients A of the involved transitions are obtained by the spectral analysis.

SUPPORTING INFORMATION

Reaction scheme for the synthesis of the chiral ligands and additional magnetic, spectroscopic, and crystallographic data.

ACKNOWLEDGMENTS

This work was supported by the French National Research Agency (ANR) through MONAFER (ANR-18-CE09-0032), and MaChiNaCo (ANR-19-CE09-0018) projects and the National Natural Science Foundation of China (Grants 92161203, 92161104, 21871224, 21721001) and Innovation Laboratory for Sciences and Technologies of Energy Materials of Fujian Province (IKKEM Grant RD2021040301).

AUTHOR INFORMATION

Corresponding Authors

*E-mail: matteo.atzori@lncmi.cnrs.fr

*E-mail: xjkong@xmu.edu.cn

Author Contributions

The manuscript was written through contributions of all authors. All authors have given approval to the final version of the manuscript. † These authors contributed equally to this work.

REFERENCES

(1) Kuang, H.; Xu, C.; Tang, Z. Emerging Chiral Materials. *Adv. Mater.* **2020**, *32*, 2005110.

(2) Ohkoshi, S.; Takano, S.; Imoto, K.; Yoshikiyo, M.; Namai, A.; Tokoro, H. 90-Degree Optical Switching of Output Second-Harmonic Light in Chiral Photomagnet. *Nat. Photonics* **2014**, *8*, 65–71.

(3) Train, C.; Gheorghe, R.; Krstic, V.; Chamoreau, L.-M.; Ovanesyan, N. S.; Rikken, G. L. J. A.; Gruselle, M.; Verdaguer, M. Strong Magneto-Chiral Dichroism in Enantiopure Chiral Ferromagnets. *Nat. Mater.* **2008**, *7*, 729–734.

(4) Yokosuk, M. O.; Kim, H.-S.; Hughey, K. D.; Kim, J.; Stier, A. v; O'Neal, K. R.; Yang, J.; Crooker, S. A.; Haule, K.; Cheong, S.-W.; Vanderbilt, D.; Musfeldt, J. L. Nonreciprocal Directional Dichroism of a Chiral Magnet in the Visible Range. *npj Quantum Mater.* **2020**, *5*, 20.

(5) Chang, G.; Wieder, B. J.; Schindler, F.; Sanchez, D. S.; Belopolski, I.; Huang, S.-M.; Singh, B.; Wu, D.; Chang, T.-R.; Neupert, T.; Xu, S.-Y.; Lin, H.; Hasan, M. Z. Topological Quantum Properties of Chiral Crystals. *Nat. Mater.* **2018**, *17*, 978–985.

(6) Galán-Mascarós, J. R. Bring to Light. *Nat. Phys.* **2015**, *11*, 7–8.

(7) Atzori, M.; Rikken, G. L. J. A.; Train, C. Magneto-Chiral Dichroism: A Playground for Molecular Chemists. *Chem. – A Eur. J.* **2020**, *26*, 9784–9791.

(8) Atzori, M.; Train, C.; Hillard, E. A.; Avarvari, N.; Rikken, G. L. J. A. Magneto-chiral Anisotropy: From Fundamentals to Perspectives. *Chirality* **2021**, *33*, 844–857.

(9) Long, J.; Ivanov, M. S.; Khomchenko, V. A.; Mamontova, E.; Thibaud, J.-M.; Rouquette, J.; Beaudhuin, M.; Granier, D.; Ferreira, R. A. S.; Carlos, L. D.; Donnadieu, B.; Henriques, M. S. C.; Paixão, J. A.; Guari, Y.; Larionova, J. Room Temperature Magnetoelectric Coupling in a Molecular Ferroelectric Ytterbium(III) Complex. *Science* **2020**, *367*, 671–676.

(10) Shen, B.; Kim, Y.; Lee, M. Supramolecular Chiral 2D Materials and Emerging Functions. *Adv. Mater.* **2020**, *32*, 1905669.

(11) Train, C.; Gruselle, M.; Verdaguer, M. The Fruitful Introduction of Chirality and Control of Absolute Configurations in Molecular Magnets. *Chem. Soc. Rev.* **2011**, *40*, 3297.

(12) Train, C.; Nuida, T.; Gheorghe, R.; Gruselle, M.; Ohkoshi, S. Large Magnetization-Induced Second Harmonic Generation in an Enantiopure Chiral Magnet. *J. Am. Chem. Soc.* **2009**, *131*, 16838–16843.

(13) Pardo, E.; Train, C.; Liu, H.; Chamoreau, L.-M.; Dkhil, B.; Boubekeur, K.; Lloret, F.; Nakatani, K.; Tokoro, H.; Ohkoshi, S.; Verdaguer, M. Multiferroics by Rational Design: Implementing Ferroelectricity in Molecule-Based Magnets. *Angew. Chemie* **2012**, *51*, 8356–8360.

(14) Barron, L. D.; Vrbancich, J. Magneto-Chiral Birefringence and Dichroism. *Mol. Phys.* **1984**, *51*, 715–730.

(15) Baranova, N. B.; Zel'Dovich, B. Ya. Theory of a New Linear Magnetorefractive Effect in Liquids. *Mol. Phys.***1979**, *38*, 1085–1098.

(16) Wagnière, G.; Meier, A. The Influence of a Static Magnetic Field on the Absorption Coefficient of a Chiral Molecule. *Chem. Phys. Lett.***1982**, *93*, 78–81.

(17) Portigal, D. L.; Burstein, E. Magneto-Spatial Dispersion Effects on the Propagation of Electro-Magnetic Radiation in Crystals. *J. Phys. Chem. Solids* **1971**, *32*, 603–608.

(18) Rikken, G. L. J. A.; Raupach, E. Pure and Cascaded Magnetochiral Anisotropy in Optical Absorption. *Phys. Rev. E* **1998**, *58*, 5081–5084.

(19) Rikken, G. L. J. A.; Raupach, E. Observation of Magneto-Chiral Dichroism. *Nature* **1997**, *390*, 493–494.

(20) Atzori, M.; Ludowieg, H.; Cortijo, M.; Breslavetz, I.; Paillot, K.; Rosa, P.; Train, C.; Autschbach, J.; Hillard, E. A.; Rikken, G. L. J. A. Validation of Microscopic Magneto-Chiral Dichroism Theory. *Sci. Adv.* **2021**, *7*, eabg2859.

(21) Taniguchi, K.; Nishio, M.; Kishiue, S.; Huang, P.-J.; Kimura, S.; Miyasaka, H. Strong Magnetochiral Dichroism for Visible Light Emission in a Rationally Designed Paramagnetic Enantiopure Molecule. *Phys. Rev. Mater.* **2019**, *3*, 45202.

(22) Ceolín, M.; Goberna-Ferrón, S.; Galán-Mascarós, J. R. Strong Hard X-Ray Magnetochiral Dichroism in Paramagnetic Enantiopure Molecules. *Adv. Mater.* **2012**, *24*, 3120–3123.

(23) Sessoli, R.; Boulon, M.-E.; Caneschi, A.; Mannini, M.; Poggini, L.; Wilhelm, F.; Rogalev, A. Strong Magneto-Chiral Dichroism in a Paramagnetic Molecular Helix Observed by Hard X-Rays. *Nat. Phys.* **2015**, *11*, 69–74.

(24) Atzori, M.; Breslavetz, I.; Paillot, K.; Inoue, K.; Rikken, G. L. J. A.; Train, C. A Chiral Prussian Blue Analogue Pushes Magneto-Chiral Dichroism Limits. *J. Am. Chem. Soc.* **2019**, *141*, 20022–20025.

(25) Taniguchi, K.; Kishiue, S.; Kimura, S.; Miyasaka, H. Local-Site Dependency of Magneto-Chiral Dichroism in Enantiopure One-Dimensional Copper(II)–Chromium(III) Coordination Polymers. *J. Phys. Soc. Japan* **2019**, *88*, 93708.

(26) Sun, B.; Liu, X.-F.; Li, X.-Y.; Zhang, Y.; Shao, X.; Yang, D.; Zhang, H.-L. Two-Dimensional Perovskite Chiral Ferromagnets. *Chem. Mater.* **2020**, *32*, 8914–8920.

(27) Gatteschi, D.; Sessoli, R.; Villain, J. *Molecular Nanomagnets*; Oxford University Press, 2006.

(28) Guo, F.-S.; Day, B. M.; Chen, Y.-C.; Tong, M.-L.; Mansikkamäki, A.; Layfield, R. A. Magnetic Hysteresis up to 80 Kelvin in a Dysprosium Metallocene Single-Molecule Magnet. *Science* **2018**, *362*, 1400–1403.

(29) Goodwin, C. A. P.; Ortu, F.; Reta, D.; Chilton, N. F.; Mills, D. P. Molecular Magnetic Hysteresis at 60 Kelvin in Dysprosocenium. *Nature* **2017**, *548*, 439–442.

(30) Gendron, F.; di Pietro, S.; Abad Galán, L.; Riobé, F.; Placide, V.; Guy, L.; Zinna, F.; di Bari, L.; Bensalah-Ledoux, A.; Guyot, Y.; Pilet, G.; Pointillart, F.; Baguenard, B.; Guy, S.; Cador, O.; Maury, O.; le Guennic, B. Luminescence, Chiroptical, Magnetic and Ab Initio Crystal-Field Characterizations of an Enantiopure Helicoidal Yb(III) Complex. *Inorg. Chem. Front.* **2021**, *8*, 914-926.

(31) Handzlik, G.; Rzepka, K.; Pinkowicz, D. The Underexplored Field of Lanthanide Complexes with Helicene Ligands: Towards Chiral Lanthanide Single Molecule Magnets. *Magnetochemistry* **2021**, *7*, 138.

(32) Li, X.-L.; Chen, C.-L.; Gao, Y.-L.; Liu, C.-M.; Feng, X.-L.; Gui, Y.-H.; Fang, S.-M. Modulation of Homochiral Dy^{III} Complexes: Single-Molecule Magnets with Ferroelectric Properties. *Chem. – A Eur. J.* **2012**, *18*, 14632–14637.

(33) Liu, C.-M.; Zhang, D.-Q.; Zhu, D.-B. Field-Induced Single-Ion Magnets Based on Enantiopure Chiral β-Diketonate Ligands. *Inorg. Chem.* **2013**, *52*, 8933–8940.

(34) Zhu, Z.; Zhao, C.; Feng, T.; Liu, X.; Ying, X.; Li, X.-L.; Zhang, Y.-Q.; Tang, J. Air-Stable Chiral Single-Molecule Magnets with Record Anisotropy Barrier Exceeding 1800 K. *J. Am. Chem. Soc.* **2021**, *143*, 10077–10082.

(35) Houard, F.; Evrard, Q.; Calvez, G.; Suffren, Y.; Daiguebonne, C.; Guillou, O.; Gendron, F.; le Guennic, B.; Guizouarn, T.; Dorcet, V.; Mannini, M.; Bernot, K. Chiral Supramolecular Nanotubes of Single-Chain Magnets. *Angew. Chemie* **2020**, *132*, 790–794.

(36) Bernot, K.; Pointillart, F.; Rosa, P.; Etienne, M.; Sessoli, R.; Gatteschi, D. Single Molecule Magnet Behaviour in Robust Dysprosium–Biradical Complexes. *Chem. Commun.* **2010**, *46*, 6458.

(37) Wang, X.-L.; Li, L.-C.; Liao, D.-Z. Slow Magnetic Relaxation in Lanthanide Complexes with Chelating Nitronyl Nitroxide Radical. *Inorg. Chem.* **2010**, *49*, 4735–4737.

(38) Atzori, M.; Dhbaibi, K.; Douib, H.; Grasser, M.; Dorcet, V.; Breslavetz, I.; Paillot, K.; Cador, O.; Rikken, G. L. J. A.; le Guennic, B.; Crassous, J.; Pointillart, F.; Train, C. Helicene-Based Ligands Enable Strong Magneto-Chiral Dichroism in a Chiral Ytterbium Complex. *J. Am. Chem. Soc.* **2021**, *143*, 2671–2675.

(39) Mitcov, D.; Platunov, M.; Buch, C. D.; Reinholdt, A.; Døssing, A. R.; Wilhelm, F.; Rogalev, A.; Piligkos, S. Hard X-Ray Magnetochiral Dichroism in a Paramagnetic Molecular 4f Complex. *Chem. Sci.* **2020**, *11*, 8306–8311.

(40) Wang, P.; Shannigrahi, S.; Yakovlev, N. L.; Hor, T. S. A. Magnetocaloric Effect of a Series of Remarkably Isostructural Intermetallic [$Ni^{II}_3Ln^{III}$] Cubane Aggregates. *Dalton Trans.* **2014**, *43*, 182–187.

(41) Peng, J.-B.; Zhang, Q.-C.; Kong, X.-J.; Zheng, Y.-Z.; Ren, Y.-P.; Long, L.-S.; Huang, R.-B.; Zheng, L.-S.; Zheng, Z. High-Nuclearity 3d–4f Clusters as Enhanced Magnetic Coolers and Molecular Magnets. *J. Am. Chem. Soc.* **2012**, *134*, 3314–3317.

(42) Moreno Pineda, E.; Chilton, N. F.; Tuna, F.; Winpenny, R. E. P.; McInnes, E. J. L. Systematic Study of a Family of Butterfly-Like {M_2Ln_2} Molecular Magnets (M = Mg^{II}, Mn^{III}, Co^{II}, Ni^{II}, and Cu^{II}; Ln = Y^{III}, Gd^{III}, Tb^{III}, Dy^{III}, Ho^{III}, and Er^{III}). *Inorg. Chem.* **2015**, *54*, 5930–5941.

(43) Chakraborty, A.; Bag, P.; Rivière, E.; Mallah, T.; Chandrasekhar, V. Assembly of Heterobimetallic Ni^{II}–Ln^{III} (Ln^{III} = Dy^{III}, Tb^{III}, Gd^{III}, Ho^{III}, Er^{III}, Y^{III}) Complexes Using a Ferrocene Ligand: Slow Relaxation of the Magnetization in Dy^{III}, Tb^{III} and Ho^{III} Analogues. *Dalton Trans.* **2014**, *43*, 8921–8932.

(44) Briganti, M.; Lucaccini, E.; Chelazzi, L.; Ciattini, S.; Sorace, L.; Sessoli, R.; Totti, F.; Perfetti, M. Magnetic Anisotropy Trends along a Full 4f-Series: The f^{n+7} Effect. *J. Am. Chem. Soc.* **2021**, *143*, 8108–8115.

(45) Yang, M. C. L.; Palmer, R. A. Natural Solid State Optical Activity of Tris(Ethylenediamine)Metal(II) Nitrates. II. Single-Crystal Circular and Linear Dichroism Spectra of Tris(Ethylenediamine)Cobalt(II) Nitrate. *J. Am. Chem. Soc.* **1975**, *97*, 5390–5395.

(46) Yang, M. C.-L.; Palmer, R. A. The Natural Optical Activity of Tris(Ethylenediamine)Metal(II) Nitrates V. The Single Crystal Circular Dichroism Spectrum of $Ni(en)_3(NO_3)_2$. *J. Chinese Chem. Soc.* **1978**, *25*, 195–201.

(47) Comba, P.; Daumann, L. J.; Klingeler, R.; Koo, C.; Riley, M. J.; Roberts, A. E.; Wadepohl, H.; Werner, J. Correlation of Structural and Magnetic Properties in a Set of Mononuclear Lanthanide Complexes. *Chem. - A Eur. J.* **2018**, *24*, 5319–5330.

(48) Comba, P.; Großhauser, M.; Klingeler, R.; Koo, C.; Lan, Y.; Müller, D.; Park, J.; Powell, A.; Riley, M. J.; Wadepohl, H. Magnetic Interactions in a Series of Homodinuclear Lanthanide Complexes. *Inorg. Chem.* **2015**, *54*, 11247–11258.

(49) Kitagawa, Y.; Wada, S.; Yanagisawa, K.; Nakanishi, T.; Fushimi, K.; Hasegawa, Y. Molecular Design Guidelines for Large Magnetic Circular Dichroism Intensities in Lanthanide Complexes. *ChemPhysChem* **2016**, *17*, 845–849.

(50) Kim, B. Y.; Yun, J.-I. Temperature Effect on Fluorescence and UV–Vis Absorption Spectroscopic Properties of Dy(III) in Molten LiCl–KCl Eutectic Salt. *J. Lumin.* **2012**, *132*, 3066–3071.

(51) Kofod, N.; Arppe-Tabbara, R.; Sørensen, T. J. Electronic Energy Levels of Dysprosium(III) Ions in Solution. Assigning the Emitting State and the Intraconfigurational 4f–4f Transitions in the Vis–NIR Region and Photophysical Characterization of Dy(III) in Water, Methanol, and Dimethyl Sulfoxide. *J. Phys. Chem. A* **2019**, *123*, 2734–2744.

(52) Malakhovskii, A. v; Sukhachev, A. L.; Strokova, A. Yu.; Gudim, I. A. Magneto-Optical Activity of f-f Transitions and Properties of 4f States in Single-Crystal DyFe. *Phys. Rev. B* **2013**, *88*, 75103.

(53) Perfetti, M.; Gysler, M.; Rechkemmer-Patalen, Y.; Zhang, P.; Taştan, H.; Fischer, F.; Netz, J.; Frey, W.; Zimmermann, L. W.; Schleid, T.; Hakl, M.; Orlita, M.; Ungur, L.; Chibotaru, L.; Brock-Nannestad, T.; Piligkos, S.; van Slageren, J. Determination of the Electronic Structure of a Dinuclear Dysprosium Single Molecule Magnet without Symmetry Idealization. *Chem. Sci.* **2019**, *10*, 2101–2110.

(54) Lindorfer, D.; Renger, T. Theory of Anisotropic Circular Dichroism of Excitonically Coupled Systems: Application to the Baseplate of Green Sulfur Bacteria. *J. Phys. Chem. B* **2018**, *122*, 2747–2756.

(55) *Comprehensive Chiroptical Spectroscopy*; Berova, N., Polavarapu, P. L., Nakanishi, K., Woody, R. W., Eds.; John Wiley & Sons, Inc.: Hoboken, NJ, USA, 2011.

(56) Richardson, F. S. Selection Rules for Lanthanide Optical Activity. *Inorg. Chem.* **1980**, *19*, 2806–2812.

(57) Zhang, Y.-J.; Wu, G.; Xu, H.; Wang, X.; Long, L.-S.; Kong, X.-J.; Zheng, L.-S. Magnetooptical Properties of Chiral [Co_2Ln] Clusters. *Inorg. Chem.* **2020**, *59*, 193–197.

(58) Wang, X.; Du, M.-H.; Xu, H.; Long, L.-S.; Kong, X.-J.; Zheng, L.-S. Cocrystallization of Chiral 3d-4f Clusters {$Mn_{10}Ln_6$} and {Mn_6Ln_2}. *Inorg. Chem.* **2021**, *60*, 5925–5930.

(59) Stephens, P. J. Theory of Magnetic Circular Dichroism. *J. Chem. Phys.* **1970**, *52*, 3489.

(60) Mason, W. R. *A Practical Guide to Magnetic Circular Dichroism Spectroscopy*; John Wiley & Sons, Inc.: Hoboken, NJ, USA, 2007.

(61) Atzori, M.; Santanni, F.; Breslavetz, I.; Paillot, K.; Caneschi, A.; Rikken, G. L. J. A.; Sessoli, R.; Train, C. Magnetic Anisotropy Drives Magnetochiral Dichroism in a Chiral Molecular Helix Probed with Visible Light. *J. Am. Chem. Soc.* **2020**, *142*, 13908–13916.

(62) Kumar, N.; Khullar, S.; Singh, Y.; Mandal, S. K. Hierarchical Importance of Coordination and Hydrogen Bonds in the Formation of Homochiral 2D Coordination Polymers and 2D Supramolecular Assemblies. *CrystEngComm* **2014**, *16*, 6730–6744.

(63) Sheldrick, G. M. Crystal Structure Refinement with SHELXL. *Acta Crystallogr. Sect. C Struct. Chem.* **2015**, *71*, 3–8.

(64) Macrae, C. F.; Edgington, P. R.; McCabe, P.; Pidcock, E.; Shields, G. P.; Taylor, R.; Towler, M.; van de Streek, J. Mercury : Visualization and Analysis of Crystal Structures. *J. Appl. Crystallogr.***2006**, *39*, 453–457.

(65) Bain, G. A.; Berry, J. F. Diamagnetic Corrections and Pascal's Constants. *J. Chem. Educ.* **2008**, *85*, 532.

(66) Kopnov, G.; Rikken, G. L. J. A. A Multichannel Magneto-Chiral Dichroism Spectrometer. *Rev. Sci. Instrum.* **2014**, *85*, 053106.

TOC Graphic